The Astrophysical Journal, 851:129 (12pp), 2017 December 20 https://doi.org/10.3847/1538-4357/aa9d1a

Weibel Instability in Hot Plasma Flows with the Production of Gamma-Rays and Electron–Positron Pairs

E. N. Nerush, D. A. Serebryakov, and I. Yu. Kostyukov
Institute of Applied Physics of the Russian Academy of Sciences, 46 Ulyanov St., Nizhny Novgorod 603950, Russia; nerush@appl.sci-nnov.ru
Received 2017 September 15; revised 2017 November 12; accepted 2017 November 22; published 2017 December 20

Abstract

We present the results of the theoretical analysis and numerical simulations of the Weibel instability in two counterstreaming hot relativistic plasma flows, for instance the flows of electron–proton plasmas with rest-mass densities $\rho \sim 10^{-4}$ g cm^{-3}, Lorentz factors $\Gamma \sim 10$, and proper temperatures $T \sim 10^{13}$ K. The instability growth rate and the filament size at the linear stage are found analytically and are in qualitative agreement with the results of three-dimensional particle-in-cell simulations. In the simulations, incoherent synchrotron emission and pair photoproduction in electromagnetic fields are taken into account. If the plasma flows are dense, fast, and hot enough, the overall energy of the synchrotron photons can be much higher than the energy of the generated electromagnetic fields. Furthermore, a sizable number of positrons can be produced due to the pair photoproduction in the generated magnetic field. We propose a rough criterion to judge copious pair production and considerable synchrotron losses. By means of this criterion, we conclude that the incoherent synchrotron emission and the pair production during the Weibel instability can have implications for the collapsar model of gamma-ray bursts.

Key words: gamma-ray burst: general – instabilities – methods: numerical – shock waves

1. Introduction

The Weibel instability (Weibel 1959) is thought to be a source of a near-equipartition magnetic field and power-law high-energy tails in electron spectra (Silva et al. 2003; Saito & Sakai 2004; Spitkovsky 2008; Nishikawa et al. 2009) in numerous astrophysical objects, e.g., gamma-ray bursts (GRBs). The magnetic field lives for a long time, due to the nonlinear growth of the field scale (Silva et al. 2003; Medvedev et al. 2005), or for even longer, due to continuous particle injection (Garasev & Derishev 2016), and ensures the prolonged synchrotron emission needed for GRB afterglow interpretation (Piran 1999). The synchrotron afterglow model explains the GRB emission fairly well, at least in the radio band (Chevalier 1998; Soderberg et al. 2010). The Weibel instability has been intensively studied theoretically (Grassi et al. 2017), numerically (including extreme laser fields; see Efimenko et al. 2017), and experimentally (Liu et al. 2011; Huntington et al. 2015; Garasev et al. 2017).

One may notice that the power of the synchrotron emission is proportional to (Landau & Lifshitz 1975) $\gamma^2 B^2$, where γ is the electron Lorentz factor and B is the magnitude of the large-scale electromagnetic fields. Thus, this power is approximately proportional to the cube of the energy density of the flows (Piran 1999), and the energy being carried away by synchrotron photons can become greater than the energy of large-scale electromagnetic fields for quite dense and energetic flows. More precisely, we consider plasmas and fields such that $\chi \sim 1$, where χ is the quantum parameter crucial for synchrotron emission (Berestetskii et al. 1982),

$$\chi = \frac{e\hbar}{m^3c^4}\sqrt{(\varepsilon_e E/c + \boldsymbol{p}_e \times \boldsymbol{B})^2 - (\boldsymbol{p}_e \cdot \boldsymbol{E})^2}\,, \tag{1}$$

where ε_e and $\boldsymbol{p}_e$ are the electron energy and momentum, $\boldsymbol{E}$ and $\boldsymbol{B}$ are the electric and magnetic field magnitudes, $\hbar$ is Planck's constant, c is the speed of light, and $e > 0$ and m are the electron charge and mass, respectively. If $\chi \gtrsim 1$, the energy of a photon emitted by an electron is about the electron energy, and the average distance at which the photon emission occurs is about $\ell_{\rm em} \sim \ell_f/\alpha$, where $\ell_f \sim mc^2/(eB)$ is the radiation formation length (Berestetskii et al. 1982) and $\alpha = e^2/\hbar c \approx 1/137$ is the fine structure constant. Hence, the ratio of $\ell_{\rm em}/c$ to the timescale of the Weibel instability (Grassi et al. 2017) is the following:

$$\frac{\ell_{\rm em}\omega}{c\bar{\gamma}_e^{1/2}} \sim \frac{1}{\alpha\bar{\gamma}_e}, \tag{2}$$

where $\omega = (4\pi e^2 n_e/m)^{1/2}$ is the electron plasma frequency, and we use the equipartition assumption $B^2 \sim 8\pi n_e mc^2\bar{\gamma}_e$, where n_e is the electron density and $\bar{\gamma}_e$ is the mean electron Lorentz factor. Equation (2) obviously means that if $\bar{\gamma}_e \gtrsim 137$ and $\chi \sim 1$ is reached, the synchrotron emission potentially can take away the electron energy on a timescale shorter than the Weibel instability timescale. Thus, synchrotron losses should be taken into account if one considers the Weibel instability in dense ultrarelativistic plasma flows.

If for an electron $\chi \sim 1$, it quite probably emits a photon with momentum $p_\gamma \sim p_e$ almost parallel to the electron momentum, $\boldsymbol{p}_\gamma \| \boldsymbol{p}_e$, and with the energy of about the electron energy (Berestetskii et al. 1982; Baier et al. 1998), $\varepsilon_\gamma \sim \varepsilon_e$. Pair photoproduction in a strong electromagnetic field,

$$\gamma \to e^+ + e^-, \tag{3}$$

is governed by the quantum parameter

$$\varkappa = \frac{e\hbar}{m^3c^4}\sqrt{(\varepsilon_\gamma E/c + \boldsymbol{p}_\gamma \times \boldsymbol{B})^2 - (\boldsymbol{p}_\gamma \cdot \boldsymbol{E})^2}\,, \tag{4}$$

which is the same as the χ in Equation (1) with ε_γ and $\boldsymbol{p}_\gamma$ substituted for by ε_e and $\boldsymbol{p}_e$, respectively. Hence, for a photon emitted by an electron with $\chi \gtrsim 1$, we estimate $\varkappa \gtrsim 1$. In this case, the probability of the pair photoproduction is of the order of the probability of the emission of a synchrotron photon by

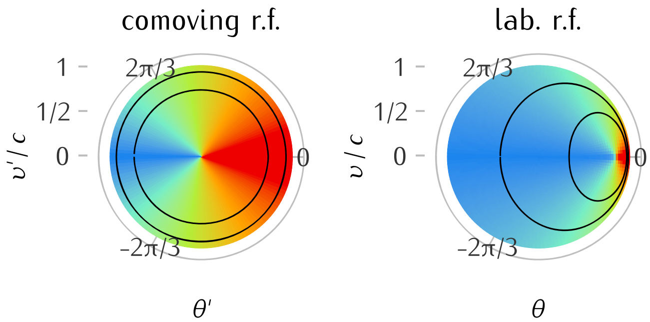

Figure 1. Mapping of the particle velocity values v' and the angles θ' (between $\boldsymbol{v}'$ and the x-axis) from the proper reference frame of the flow (K', left) to the laboratory reference frame (K, right). Different values of θ' are shown with different colors, and the left panel depicts the color bar for the right one; the radial coordinate depicts either the velocity v' (left) or v (right). The x-axis is parallel to the direction of $\boldsymbol{V}$, where $\boldsymbol{V}$ is the velocity of K' in K. For this plot, $V = 0.86\,c$.

the electron. Therefore, pair production (Equation (3)) should be also taken into account.

Here we present the results of numerical simulations of the Weibel instability in two counterstreaming hot and dense relativistic plasma flows. The simulations were performed with the particle-in-cell (PIC) code QUILL (Nerush & Kostyukov 2010; Serebryakov et al. 2015), utilizing the Monte Carlo technique (Nerush et al. 2014) together with Baier–Katkov quasiclassical formulas (Berestetskii et al. 1982; Baier et al. 1998; for PIC codes with pair production, see also, e.g., Grismayer et al. 2017, Kalapotharakos et al. 2017). The code QUILL conserves the sum energy of fields and particles that allows, for instance, the laser field absorption in a self-generated pair plasma (Nerush et al. 2011) to be simulated. Unlike synchrotron emission and pair production, particle collisions (e.g., Compton scattering and bremsstrahlung) are not included in the simulations.

Let us also note that in the theoretical considerations of the Weibel instability, we follow the electromagnetic scenario (Stockem et al. 2014), because for ultrarelativistic flows ($\Gamma \gg 1$, where Γ is the Lorentz factor of a flow in some, e.g., laboratory, reference frame K), almost all velocity vectors of plasma particles belong to a cone $\theta \lesssim 1/\Gamma$ despite the high temperature of the flow (see Figure 1; here, θ is the angle between the particle velocity and the flow velocity). This is true even if the mean Lorentz factor of the flow particles in the comoving reference frame K' is much greater than Γ, which is evident from the Lorentz transform of angles from the proper reference frame of the flow K' to K:

$$\tan\theta = \frac{v_x'}{\Gamma(v_x' + V)}\tan\theta', \tag{5}$$

where V is the flow velocity in K and the x-axis is parallel to it. Furthermore, it follows from the transformation of the Lorentz factor,

$$\gamma = \gamma'\Gamma(1 + v_x' V), \tag{6}$$

that the proper temperature of the flow determines only the mean energy of particles in the laboratory reference frame, $\bar{\gamma} = \bar{\gamma}'\Gamma$ (we assume $\overline{v_x'} = 0$). Therefore, a hot plasma flow with $\Gamma \gg 1$ should behave similarly to a cold plasma flow, and the Weibel instability in the counterstreaming flows should grow in accordance with the electromagnetic scenario (formation and growth of current filaments with azimuthal magnetic field and low electric field; see Stockem et al. 2014; Garasev et al. 2017 and references wherein) rather than with the electrostatic one.

This paper is organized as follows. In Section 2.1, we consider the Weibel instability of the electromagnetic type in counterstreaming relativistically hot plasma flows analytically, without synchrotron emission and pair production taken into account. In Section 2.2, we estimate the plasma parameters corresponding to $\chi \sim 1$ and $\varkappa \sim 1$, hence, to efficient synchrotron emission and copious pair production. In Section 3, the results of numerical simulations with synchrotron emission and pair production taken into account are given, and in Section 4, their astrophysical implications are discussed. In Section 5, the summary of the paper is given.

2. Weibel Instability in Hot Collisionless Plasmas

2.1. Effect of Temperature

Let us consider the stability of two relativistic counterpropagating plasma flows moving along the x-axis with respect to the formation of a cylindrically symmetric current filament. In the following, the properties of the flows are denoted by the indices 1 (the flow velocity $v_x > 0$) and 2 ($v_x < 0$). We also assume that the filament remains quasi-neutral and

$$\delta n_{e1} = \delta n_{i2} = -\delta n_{i1} = -\delta n_{e2}, \tag{7}$$

where δn is the density perturbation relative to the initial value for the flow (n_1 or n_2) and the indices i and e refer to protons and electrons, respectively (assumption (7) will be justified a bit later; it is not always fulfilled and is used to simplify calculations). Let r and φ be the cylindrical coordinates with respect to the axis of the current filament that coincides with the x-axis. x, r, and φ are right-handed coordinates. We also assume that none of the plasma characteristics depend on x, therefore Maxwell's equations can be written as follows:

$$\frac{\partial E_x}{\partial t} = \frac{c}{r}\frac{\partial(rB_\varphi)}{\partial r} + 16\pi ec\delta n_{e1}, \tag{8}$$

$$\frac{\partial B_\varphi}{\partial t} = c\frac{\partial E_x}{\partial r}. \tag{9}$$

To obtain the equation for the density perturbation, one should start from the Boltzmann equation in Cartesian coordinates:

$$\frac{\partial f}{\partial t} + (\boldsymbol{v}, \nabla)f + \frac{(\boldsymbol{F}, \nabla_v)}{m\gamma}f = 0, \tag{10}$$

where $f(\boldsymbol{r}, \boldsymbol{v})$ is the distribution function, $\gamma = (1 - v^2)^{1/2}$, and we assume that for particles $\boldsymbol{F} \perp \boldsymbol{v}$, hence $d\gamma/dt = 0$. For the particle density,

$$n(y, z) = \iiint_{v^2<c^2} f(y, z, v_x, v_y, v_z)\, dv_x\, dv_y\, dv_z. \tag{11}$$

From the Boltzmann equation, we obtain

$$\frac{\partial n}{\partial t} = -\nabla\cdot(n\bar{\boldsymbol{v}}), \tag{12}$$

where the bar denotes averaging over velocities:

$$\bar{a} = \frac{1}{n} \iiint_{v^2<c^2} af \, dv_x \, dv_y \, dv_z. \tag{13}$$

For the average velocity, we obtain

$$\frac{\partial \bar{v}_k}{\partial t} = \overline{\left(\frac{F_k}{m\gamma}\right)} - \bar{v}_l \frac{\partial \bar{v}_k}{\partial x_l} - \frac{1}{n}\frac{\partial}{\partial x_l}[\overline{(v_l - \bar{v}_l)(v_k - \bar{v}_k)}n], \tag{14}$$

where the Einstein summation convention is used. We also assume that the covariance matrix for $\boldsymbol{v}$ is a constant, i.e.,

$$\mathcal{V}_{kl} \equiv \overline{(v_k - \bar{v}_k)(v_l - \bar{v}_l)} = \text{const}, \tag{15}$$

and the distribution function is assumed to be symmetrical in the yz coordinates, so that $\mathcal{V}_{k\neq l} = 0$ and $\mathcal{V}_{zz} = \mathcal{V}_{yy} \equiv \mathcal{V}$. Then, Equation (14) for v_y or v_z can be written as

$$\frac{\partial \bar{v}_k}{\partial t} = \overline{\left(\frac{F_k}{m\gamma}\right)} - \bar{v}_l \frac{\partial \bar{v}_k}{\partial x_l} - \frac{\mathcal{V}}{n}\frac{\partial n}{\partial x_k}. \tag{16}$$

We suppose that in the case of a relativistically hot plasma in the proper reference frame, the plasma particles are uniformly distributed over the surface of a sphere $v_x'^2 + v_y'^2 + v_z'^2 \simeq c^2$, hence, using velocity transformation formulas,

$$v_x = \frac{v_x' + V}{1 + v_x' V/c^2} \tag{17}$$

$$v_{y,z} = \frac{v_{y,z}'\sqrt{1 - V^2/c^2}}{1 + v_x' V/c^2}, \tag{18}$$

one may easily derive the expression for $\mathcal{V}$ in the reference frame where the flow velocity is relativistic:

$$\mathcal{V} \simeq \frac{1}{\Gamma^2} \iint_{v_y'^2+v_z'^2<c^2} \frac{v_y'^2}{v_x'(1 + v_x'/c)^2} \, dv_y' \, dv_z' \times \left(\iint_{v_y'^2+v_z'^2<c^2} \frac{1}{v_x'} \, dv_y' \, dv_z'\right)^{-1} \approx \frac{0.2c^2}{\Gamma^2}. \tag{19}$$

Here, $v_x' = (c^2 - v_y'^2 - v_z'^2)^{1/2}$.

After that, Equations (12) and (16) can be rewritten in cylindrical coordinates, assuming that $\bar{v}_\varphi = 0$:

$$\frac{\partial n}{\partial t} = -\frac{1}{r}\frac{\partial (rn\bar{v}_r)}{\partial r}, \tag{20}$$

$$\frac{\partial \bar{v}_r}{\partial t} = \overline{\left(\frac{F_r}{m\gamma}\right)} - \bar{v}_r \frac{\partial \bar{v}_r}{\partial r} - \frac{\mathcal{V}}{n}\frac{\partial n}{\partial r}. \tag{21}$$

We consider only the initial stage of the instability, so for the force in Equation (21), the following expression can be used:

$$\bar{F}_r \simeq \pm eB_\varphi, \tag{22}$$

where the sign is determined by the sign of $\bar{v}_x$ and the sign of the particle charge, hence we can estimate

$$\overline{\left(\frac{F_r}{m\gamma}\right)} \simeq \frac{\bar{F}_r}{m\bar{\gamma}}. \tag{23}$$

Notice that the sign of the force is the same for the ions (electrons) of the first flow and for the electrons (ions) of the second flow, so in the case of flows with equal densities, Lorentz factors, and temperatures, the density is perturbed such that the quasi-neutrality condition, Equation (7), stands true. Otherwise, when the densities or Lorentz factors of the flows do not coincide, condition (7) may not be fulfilled, but we will use it for the sake of simplicity, assuming the plasma is quasi-neutral.

We look for the solution of Maxwell's Equations (8) and (9) together with Equations (20) and (21) in the following form:

$$E_x = E_0 e^{\Lambda t} J_0(r/\lambda), \tag{24}$$

$$\delta n_{e1} = -\delta n_0 e^{\Lambda t} J_0(r/\lambda), \tag{25}$$

$$v_r \propto B_\varphi \propto e^{\Lambda t}\frac{dJ_0(r/\lambda)}{dr}, \tag{26}$$

where E_0 and δn_0 are the amplitudes and J_0 is the zero-order Bessel function of the first kind, i.e., the solution of the equation

$$\frac{1}{r}\frac{d}{dr}\left\{r\frac{d[rJ_0(r/\lambda)]}{dr}\right\} = -\frac{1}{\lambda}J_0(r/\lambda). \tag{27}$$

Therefore, we obtain the equations that describe the parameters of the cylindrically symmetric mode:

$$\left(1 - \frac{4\omega_1^2}{\bar{\gamma}_1\Lambda^2}\right)\frac{c^2}{\lambda^2}E_0 + \Lambda^2 E_0 + \frac{16\pi ec\mathcal{V}_1}{\Lambda\lambda^2}\delta n_0 = 0, \tag{28}$$

$$\frac{\mathcal{V}_1}{\lambda^2}\delta n_0 - \frac{n_1 ec}{\Lambda m\bar{\gamma}_1}\frac{1}{\lambda^2}E_0 + \Lambda^2\delta n_0 = 0, \tag{29}$$

where n_1, again, is the first flow initial density $n_1 \equiv n_{e,1}(t = 0)$ and $\omega_1 = (4\pi e^2 n_1/m)^{1/2}$ is the related plasma frequency.

The first equation at $\mathcal{V} = 0$ describes, in addition to the stable mode, the Weibel instability, and the second at $E_0 = 0$ describes quasi-sound waves. In the first and second cases, it is easy to obtain a relation between the characteristic spatial scale of the mode λ and the characteristic "increment" Λ:

$$\Lambda^2_{\mathcal{V}=0} = \frac{c^2}{2\lambda^2}\left(-1 \pm \sqrt{1 + \frac{16\lambda^2\omega_1^2}{c^2\bar{\gamma}_1}}\right), \tag{30}$$

$$\Lambda^2_{E_0=0} = -\frac{\mathcal{V}_1}{\lambda^2}. \tag{31}$$

The relation between Λ and λ can be found from Equations (30) and (31) in the general case as well:

$$\Lambda^4 + \frac{c^2 + \mathcal{V}_1}{\lambda^2}\Lambda^2 - \frac{c^2}{\lambda^2}\left(\frac{4\omega_1}{\bar{\gamma}_1} - \frac{\mathcal{V}_1}{\lambda^2}\right) = 0, \tag{32}$$

therefore, taking into account that $\mathcal{V}_1 \ll c^2$, we derive for the unstable mode

$$\Lambda^2 = \frac{c^2}{2\lambda^2}\left(-1 + \sqrt{1 + \frac{4\lambda^2}{c^2}\left(\frac{4\omega_1^2}{\bar{\gamma}_1} - \frac{\mathcal{V}_1}{\lambda^2}\right)}\right). \tag{33}$$

In the above equation, it can be seen that at $\mathcal{V} \neq 0$, the considered mode is unstable ($\Lambda^2 > 0$) if

$$\lambda > \frac{\sqrt{\bar{\gamma}_1\mathcal{V}_1}}{2\omega_1}, \tag{34}$$

i.e., for modes with a spatial scale greater than a few. It can be easily shown that in the presence of temperature, the maximum increment Λ_m is realized for the mode with the following spatial scale,

$$\lambda_m^2 \sim \mathcal{V}_1 \bar{\gamma}_1 / \omega_1^2, \quad \frac{\lambda_m}{\lambda_1} \sim \frac{1}{2\pi} \frac{\bar{\gamma}_1^{1/2}}{\Gamma_1}, \tag{35}$$

and equals

$$2\pi \Lambda_m / \omega_1 \sim 2\pi / \sqrt{\bar{\gamma}_1}. \tag{36}$$

Note that although we obtain Equations (35) and (36) for flows with equal parameters, we will use these equations for flows with different parameters as well, assuming that the index 1 denotes the flow with a higher corrected plasma frequency, $\omega_1 / \bar{\gamma}_1^{1/2} > \omega_2 / \bar{\gamma}_2^{1/2}$, which yields a higher value for the increment (Equation (36)). The obtained estimates are compared with the results of the numerical simulations in Section 3.

2.2. Pair Production

Here we consider pair photoproduction, Equation (3), in electromagnetic fields during the Weibel instability. The pair production becomes efficient if $\varkappa \gtrsim 1$, where the quantum parameter $\varkappa$ depends on the field magnitude and the energy of the photon; see Equation (4). In order to check if the process (Equation (3)) appears in some astrophysical objects, the magnitude of the electromagnetic fields and photon energy should be found.

For the sake of simplicity, we consider the Weibel instability in two counterstreaming plasma flows in the reference frame where the momentum flow is the same for both jets:

$$n_1 \Gamma_1 V_1^2 \eta_1 \simeq n_2 \Gamma_2 V_2^2 \eta_2. \tag{37}$$

Here, we estimate $\bar{\gamma}_1 \approx \Gamma_1 \eta_1$ and $\bar{\gamma}_2 \approx \Gamma_2 \eta_2$. The parameter η defines the average kinetic energy of ions in the reference frame comoving with the flow as follows:

$$\eta = \overline{(\gamma_i - 1)}. \tag{38}$$

From here on, we assume that flow 1 is denser than flow 2 ($n_1 > n_2$), and in flow 2, ions and electrons are more energetic than those in flow 1 ($\bar{\gamma}_2 \gtrsim \bar{\gamma}_1$).

We assume that a sizable part of the initial energy of the flows is transferred to the energy of the electromagnetic fields, and the magnitude of the fields can be estimated as follows:

$$B^2 \sim 8\pi n_2 mc^2 \bar{\gamma}_2, \tag{39}$$

where we additionally suppose that the volume occupied by the plasma is not changed much while the filaments grow. An electron in strong-enough fields emits photons with energy of about its own energy (namely, if $\chi \gtrsim 1$; see Section 1). Therefore, in $\varkappa$ (Equation (4)), we can estimate the photon energy as follows:

$$\varepsilon_\gamma \sim mc^2 \bar{\gamma}_2, \tag{40}$$

which leads to

$$\varkappa \sim \bar{\gamma}_2^{3/2} \sqrt{8\pi n_2 r_e \lambda_C^2}, \tag{41}$$

where $r_e = e^2/mc^2$ is the classical electron radius and $\lambda_C = \hbar/mc$ is the Compton wavelength. Supposing that the average electron energy initially or after the acceleration process (Silva et al. 2003; Spitkovsky 2008) is as high as the initial ion energy, we have $\bar{\gamma}_2 \approx \Gamma_2 \eta_2 M/m$. Therefore, copious pair production is ensured if

$$\varkappa \sim (\eta_2 \Gamma_2 M/m)^{3/2} \sqrt{8\pi n_2 r_e \lambda_C^2} \gtrsim 1. \tag{42}$$

Here, again, all values are given in the center-of-momentum reference frame (37) and the index 2 denotes the flow with particle density lower than the density of the other flow.

In the case of strong synchrotron losses, the equipartition assumption can lead to an overestimation of the magnitude of the fields. On the other hand, we estimate the photon energy using the mean particle energy and do not take into account high-energy spectrum tails (Silva et al. 2003; Spitkovsky 2008). However, the resulting criterion of copious pair production, Equation (42), can remain relevant despite the losses; this is confirmed in the next section by means of numerical simulations.

3. Results of Numerical Simulations

To verify the above estimates, we performed three-dimensional numerical simulations of the development of the Weibel instability in counterpropagating hot plasma flows using the PIC code QUILL (Nerush & Kostyukov 2010; Serebryakov et al. 2015). To numerically solve kinetic equations, PIC simulations in which distribution functions are represented as sums of quasiparticle shape functions are generally used (Pukhov 2003; Birdsall & Langdon 2004), and Maxwell's equations are solved with finite-difference schemes. In QUILL, the algorithms of Pukhov (1999) are used in order to solve Maxwell's equations and to approximate currents and fields. In order to solve the equations of quasiparticle motion, we used the method of Vay (2008).

The simulations were carried out taking into account the emission of hard photons and pair photoproduction in strong fields by means of the Monte Carlo method. Namely, for a quasiparticle (e.g., an electron), at every time step, two random numbers (one relates to the emitted photon energy and the other to the emission probability), which are used to make decision on the photon emission (Elkina et al. 2011), are generated. Then, if photon emission occurs, a new quasiparticle (hard photon with the same position as of the emitting electron) is added to the simulation region, and the electron momentum is decreased by the momentum of the emitted photon. Pair photoproduction is treated similarly. The method described leads to the correct energy transfer between fields, particles, and secondary particles, and the QUILL code is capable of simulating, for instance, the field absorption in self-sustained electromagnetic cascades (Nerush et al. 2011) or the influence of synchrotron losses on the ion acceleration by the laser field (Nerush & Kostyukov 2015; Artemenko et al. 2016).

Using the classical description of the electron trajectory together with quantum synchrotron formulas for the photon emission and pair production is valid because the radiation formation length in strong-enough fields is much smaller than the field characteristic scale (Landau & Lifshitz 1975; Baier et al. 1998), thanks to a spectral gap between the large-scale electromagnetic fields and synchrotron photons (Gonoskov et al. 2015). It is worth noting that collisions of particles and, in particular, Compton scattering and bremsstrahlung were not taken into account.

The simulations performed were three dimensional, and the quasiparticle merging algorithm (the algorithm that reduces the number of particles in the simulation domain; see Timokhin

Table 1
Simulation Parameters and Results

Simulation	n_1 (cm^{-3})	η_1	Γ_1	n_2/n_1	η_2	Γ_2	M/m	λ_m/λ_1	$2\pi\Lambda_m/\omega_1$	$\varkappa$	N_p/N_e	dN_p/dN_γ
s1	1×10^{25}	2	25	0.25	20	10	10	0.14	0.28	14	1.4×10^{-3}	6×10^{-3}
s2$_{26}$	6.3×10^{23}	20	10	1	20	10	10	0.71	0.14	7.2	1.4×10^{-3}	3×10^{-3}
s3	2.5×10^{24}	5	10	0.4	5	25	1	0.11	0.89	0.14	1.5×10^{-7}	$<10^{-6}$
s4$_{22}$	1.6×10^{23}	1.3	10	1	1.3	10	15	0.22	0.45	0.11	1.4×10^{-8}	$<10^{-6}$
s5	7.7×10^{22}	10	16	0.5	2	160	15	0.49	0.13	6.5	7×10^{-6}	7×10^{-5}
s6$_{23}$	1.9×10^{22}	7	4	0.7	4	10	20	0.94	0.27	0.27	3.6×10^{-9}	$<10^{-6}$
s7	5×10^{24}	2	4	0.08	1.2	80	20	0.5	0.5	5.7	3.8×10^{-6}	1×10^{-4}

2010), implemented in QUILL, was not used. In comparison with two-dimensional simulations with merging of quasiparticles, our setup obviously requires much more computational resources. This limits the simulation resolution and the computational time (see below); nevertheless, this fits better the aims of the simulations, i.e., first, it clearly demonstrates the electromagnetic nature of the Weibel instability for the considered parameters, and, second, it clearly demonstrates that the criterion given by Equation (42) is reasonable. Two-dimensional simulations, in that $\varkappa \gg 1$ and the saturation of the Weibel instability are reached, will be considered in further publications.

We chose the following simulation parameters: the size of the simulation region was $54 \times 24 \times 24\, \lambda_1^3$, where λ_1, as before, is the plasma wavelength of the denser flow. Initially, each of the flows occupied half of the region. The transverse step of the numerical grid was equal to $\Delta y = \Delta z = 0.14\, \lambda_1$, the longitudinal one was $\Delta x = 0.063\, \lambda_1$, and the time step was $\Delta t = 0.06 \times 2\pi/\omega_1$. The initial number of quasiparticles of each species (electrons and ions) in a cell is equal to eight. The plasma density of the flows had a flat transverse profile with a decrease in the density at the edges to zero on the scale $\sim 2\, \lambda_1$. We used open boundary conditions that allowed the free outflow of electromagnetic waves and particles at the boundaries (Pukhov 1999).

Initially, the particles of the flow in the comoving reference frame had the distribution

$$f_i \propto e^{-(\gamma-1)/\eta}, \tag{43}$$

$$f_e \propto e^{-m(\gamma-1)/(M\eta)}, \tag{44}$$

hence, the average kinetic energy of the ions (or the electrons) in the comoving reference frame was equal to $Mc^2\eta$.

We carried out a series of seven simulations for different Lorentz factors, densities, and temperatures of the plasma flows, which were chosen randomly. The parameters of the simulations are given in Table 1, where s* denotes the simulation identifier. The proton-to-electron mass ratio M/m in the simulations was chosen to be much lower than that for the real particles in order to reduce computational costs. For the given parameters of the simulations, the instability growth rate Λ_m and the transverse scale of the filaments λ_m were computed using Equations (36) and (35), respectively. The parameter $\varkappa$, crucial for pair photoproduction, was estimated using Equation (42). In most simulations, the end time was equal to $t_{\mathrm{end}} = 27 \times 2\pi/\omega_1$. However, in some simulations, we were forced to terminate them before t_{end} due to the significant growth of the number of particles (mostly photons). In those simulations, the end time is given as a subscript in a simulation identifier (e.g., s4$_{22}$). The ratio of the number of positrons to the number of electrons N_p/N_e at the end of a simulation and the quantity dN_p/dN_γ characterizing the positron generation efficiency (see more details further) are computed in the simulations and are also given in Table 1.

Let us consider the s2 simulation as an example. Figure 2(a) shows the sum of the electron and ion density (shown as the color intensity) as well as the relative electric charge (shown as color hue) at the filament cross-section. It is seen that the plasma remains close to neutral during the instability growth. Figure 2(b) depicts the transverse (azimuthal) magnetic field generated around the filaments. It should be noted that the typical filament size and the scale of the magnetic field they generate are approximately of the order of the distance between the filaments. From Figures 2(c) and (d), showing the electron and photon density distributions, respectively, one can see that the positions of these distributions' maxima coincide. At the same time, the distribution of the generated positrons is similar to the distribution of the magnetic field (see Figures 2(b), (c), and (e)).

In Figure 3 (top), the growth of the energy of electromagnetic fields, the growth of the energy of photons and positrons in the process of instability development in the s2 simulation, are shown with solid lines (for comparison, the dashed lines show the same quantities for the s3 simulation). Figure 3 (bottom) depicts the number of electrons, positrons, and synchrotron photons in the s2 and s3 simulations as functions of time. Despite the fact that the energy of the electromagnetic fields in the s3 simulation is higher, the number of positrons produced in it is negligible in comparison with the s2 simulation. It can be seen from Figure 3 (top) that the growth rate of the plasma field energy (i.e., the slope of the f lines) depends on time, which is explained by the transition from the linear stage of the instability development to the nonlinear one. The nonlinear stage is characterized not only by the perturbation of the plasma density of the order of its initial value, but also by the merging of the current filaments. As an example, see the density distribution in the y–z plane for the s3 simulation at two different time instants (Figure 4).

Consider the entire set of simulation results (s1–s7). The characteristic transverse scale of the filaments ℓ was found from the simulation results as follows. First, the modulus of the Fourier image of B_y in the y–z plane was computed, and its background (values below 0.1 of its maximum) was deleted. Figure 5(a) shows such a Fourier image for the s3 simulation and $t = 10\lambda_1/c$. Then, using this image, the dispersion of the transverse wave vectors was computed, for example, Figure 5(a) yields the dispersion $k^2 \approx 9.7/\lambda_1^2$ and therefore $\ell = 2\pi/k \approx 2\lambda_1$.

For the s1–s7 simulations, the characteristic distance between the filaments ℓ computed with this method as a

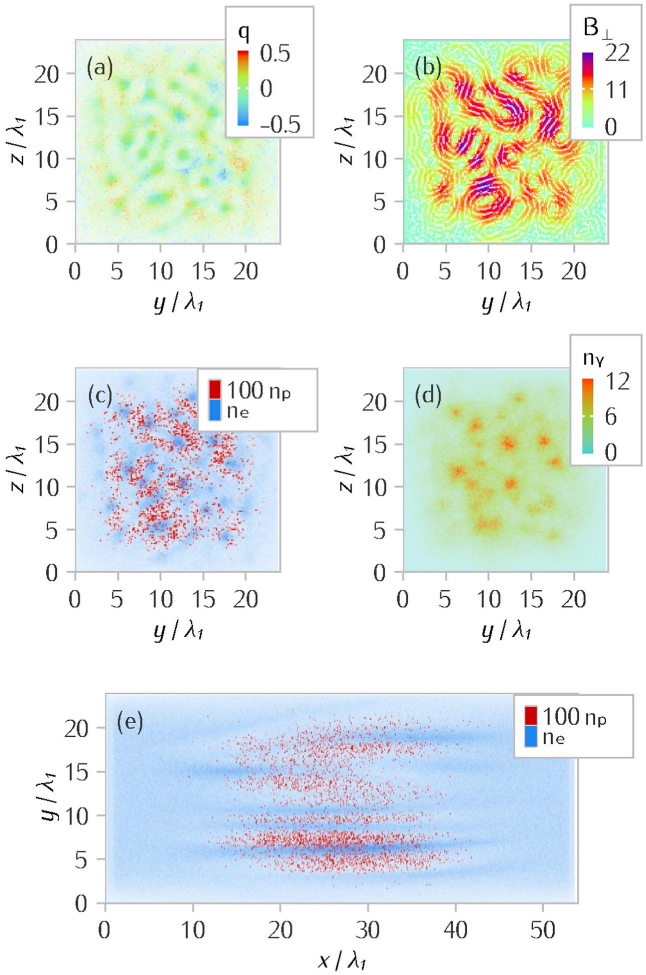

Figure 2. Results of the s2 simulation. (a) In the y–z plane, the sum of the proton and electron density is shown with the color intensity, and the ratio of the charge density to the total particle density is depicted as the color hue (q; the red color corresponds to a plasma consisting of 60% ions and 30% electrons, the blue color corresponds to a 30% ion and 60% electron mixture; see also Figure 4). (b) The transverse magnetic field $(B_y^2 + B_z^2)^{1/2}$ distribution in the y–z plane; white lines sketchily show the field direction. The electron and positron density distribution (c) in the y–z and (e) in the x–y planes. Note that the maximum positron density is about two orders of magnitude lower than that of electrons. (d) The gamma quanta density in the y–z plane. All distributions are given at $t = 26\lambda_1/c$. Both the x–y plane and the y–z plane pass through the center of the simulation area.

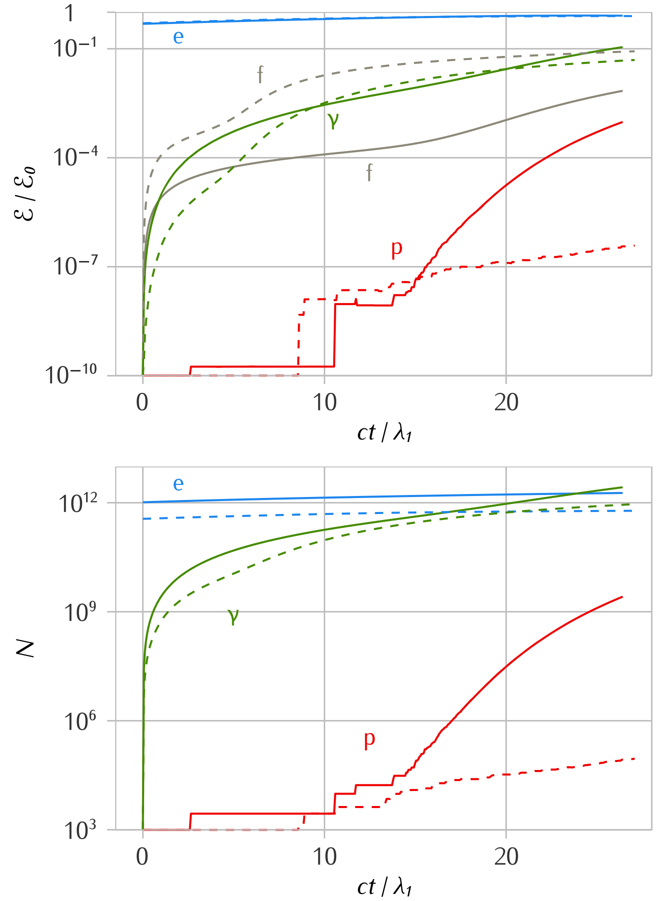

Figure 3. Normalized particle and field energy (top) and the particle number (bottom), as they depend on time in two different simulations: s2 (solid lines) and s3 (dashed lines). $\mathcal{E}_0$ is the initial overall energy of ions in the simulation box, multiplied by 2. Electrons (e), positrons (p), photons (γ), and electromagnetic fields (f) are shown.

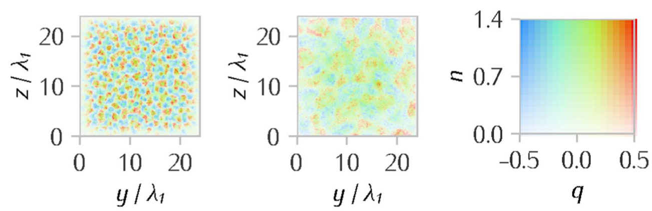

Figure 4. Total electron and ion density $n = (n_e + n_i)/4n_1$ and the relative charge density $q = (n_i - n_e)/(n_i + n_e)$ for the s3 simulation at different time instants: $t = 10\lambda_1/c$ (left) and $t = 20\lambda_1/c$ (middle). The right panel shows the color correspondence for different n and q values. The same color correspondence is used in Figure 2(a).

function of time is given in Figure 5(b). The dependence of the energy of hard photons $\mathcal{E}_\gamma$ and the dependence of the energy of the electromagnetic field $\mathcal{E}_{\rm em}$ on time are depicted in Figures 5(c) and (d), respectively.

In small times, the magnetic field generated due to the Weibel instability is smaller than the noise associated with the temperature, so the described method of filament scale computation gives an ℓ of the order of the transverse step of the numerical grid. However, if the generated magnetic field becomes greater than the noise level, the sharp growth of ℓ from the grid step to some other value occurs. We suppose that the value of ℓ computed at the end of this sharp growth corresponds to the filament scale reasonably well. The time instants of this sharp growth and the resulting transverse scales of the filaments for the s1–s7 simulations are shown in Figure 5(b) with dots, together with the estimated value of the filament size $5\lambda_m$ computed with Equation (35) and marked with the short black lines. We multiplied the analytical values λ_m by 5 for better coincidence between theory and simulations. The need for this multiplier can be explained by the fact that Equation (35) gives the filament radius whereas the method of ℓ computation instead gives the distance between filaments. Note that the filament size computed for the s1 and s3 simulations is close to the step size of the numerical grid, and thus, in these simulations, the linear stage of the Weibel instability was computed with a higher inaccuracy than in the others.

The nonlinear stage of development of the Weibel instability is characterized, first, by the fact that the density perturbation becomes of the order of the initial particle density and, second, by the filament merging. In Figure 5(b), almost for all

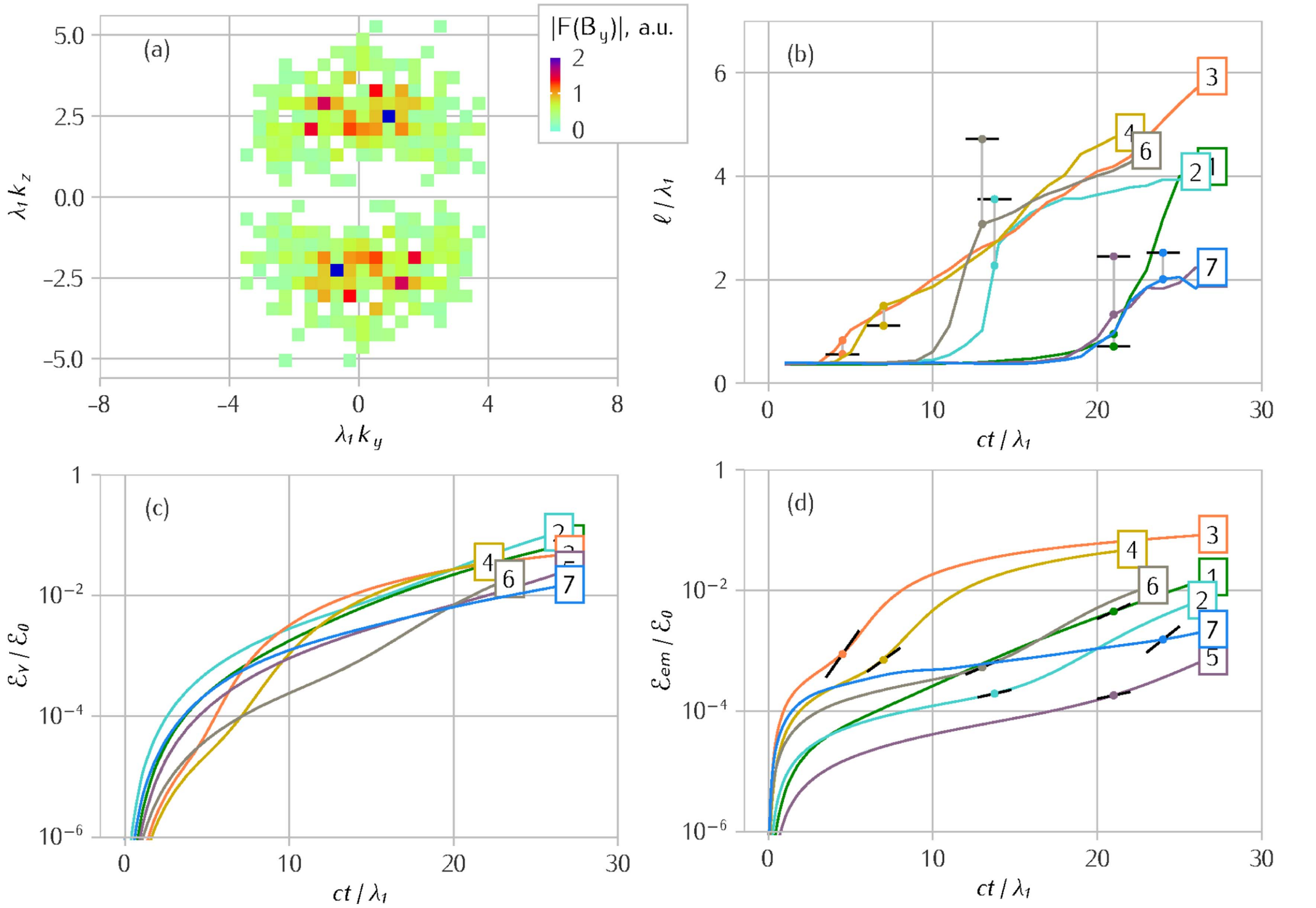

Figure 5. (a) Modulus of the two-dimensional Fourier image of the magnetic field component $B_y(y, z)$, $|F(B_y)|$, in the simulation s3 at $t = 10\lambda_1/c$ and at x passing the center of the simulation box; k_y and k_z are the wavenumbers along the y- and the z-axes respectively. (b) For the s1–s7 simulations, the filament size ℓ determined from the Fourier images of B_y, as a function of time. Dots mark the time instants at which the determination of the filament size from $|F(B_y)|$ starts to be relevant. The ordinate of the black horizontal bars corresponds to the estimate of the filament scale, Equation (35), multiplied by 5, i.e., $5\lambda_m/\lambda_1$ (see Table 1 for the numerical values). (c) The energy of the gamma-rays and (d) the energy of the large-scale electromagnetic fields normalized to the ion energy of the unperturbed flows that fill up the simulation box entirely, $\mathcal{E}_0$. The short black lines in (d) are the exponents $\mathcal{E}_{\rm em} \propto \exp\Lambda_m t$, where Λ_m is the estimate of the instability growth rate, Equation (36) (see Table 1 for the numerical values).

simulations, the nonlinear stage starts right after the marked time instants and manifests itself as the subsequent growth of ℓ.

As Figure 5(d) and Table 1 demonstrate, by an order of magnitude, the increment at the linear stage of instability development, obtained in the numerical simulations, is in good agreement with the increment estimated with Equation (36), which does not take into account many factors. For example, in the case of essentially different parameters of flow 1 and flow 2, the difference in the density of protons and electrons in filaments can be of the order of the particle density itself (see Figure 4). In addition, the energy of the emitted gamma quanta can significantly exceed the energy of the generated electromagnetic fields even at the initial stage of instability development (see Figure 3). Equation (36) probably remains relevant in this case due to the following competing effects. On the one hand, the radiation losses decrease the particle energy that should increase the instability increment; on the other hand, electrons with lower energy become thermal earlier and no longer pump the instability.

At the saturation of the Weibel instability, in the case of counterstreaming plasma flows, the filament current is determined only by the plasma density, and the maximum magnetic field is about $B \sim n_e \ell$. Therefore, the filament size is strongly coupled with the energy of the magnetic field. Therefore, the synchrotron emission should also lead to a smaller filament radius, because the radiation losses reduce the energy of the magnetic field.

For the s2–s6 simulations, a noticeable increase in the instability increment is observed during the transition to the nonlinear stage (after the time instants marked with dots in Figure 5(d)), but after that, the increment can decrease because the filaments grow and the characteristic distance between them increases. It should also be noted that a rapid change in the filament configuration at the nonlinear stage (filament merging) can lead to the appearance of strong electric fields.

Numerical simulations in this work were carried out at the limit of technical capabilities available to the authors. Several calculations were stopped at $t < 27\lambda_1/c$ (until the flows intersected each other completely in the simulation region) because of the large number of newly born photons and limited RAM resources. Because of this, the saturation of the Weibel instability was not attained in almost all calculations; however, in all calculations, a nonlinear stage of the instability was achieved (see Figure 5). Since the simulation parameters are different and the simulation time is sometimes less than desired, we introduced the parameter

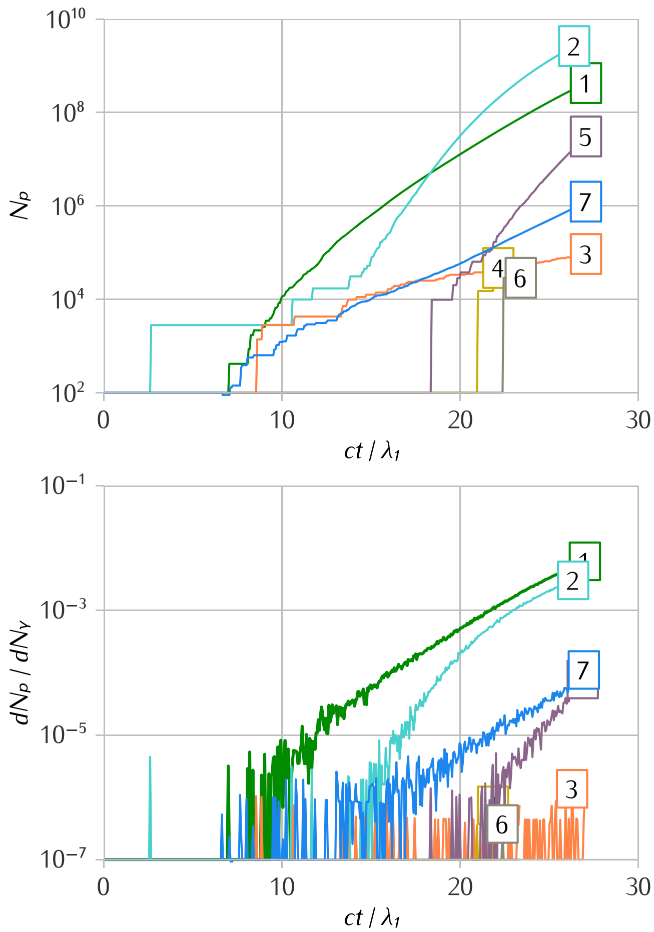

Figure 6. (Top) Number of positrons N_p and (bottom) the parameter dN_p/dN_γ in the s1–s7 simulations as functions of time.

$dN_p/dN_\gamma = (dN_p/dt)/(dN_\gamma/dt)$ in order to isolate the simulations with abundant positron production. This parameter roughly shows the proportion of photons that produce electron–positron pairs. The dependence of the number of positrons and dN_p/dN_γ on time in the s1–s7 simulations is shown in Figure 6 top and bottom, respectively. From N_p and dN_p/dN_γ at the end of the simulations (see Table 1), we conclude that in the simulations s1, s2, s5, and s7, significant production of electron–positron pairs is realized. In the s3, s4, and s6 simulations, a low number of positrons is observed (despite the significant number of photons), and dN_p/dN_γ does not exceed the background noise values. Thus, the criterion given in Equation (42), yielding $\varkappa > 1$ for the s1, s2, s5, and s7 simulations and $\varkappa < 1$ for the s3, s4, and s6 simulations, does indeed allow us to distinguish the pair production regime during the development of the Weibel instability.

4. Discussion and Astrophysical Implications

In this paper, we consider the Weibel instability in two relativistic plasma flows that can lead to efficient synchrotron emission. The numerical simulations demonstrate that the conversion efficiency of the energy of the initial flows into the energy of synchrotron photons is much higher than that for the generation of large-scale magnetic fields, if the flows are quite dense and energetic.

The numerical simulations also show that the synchrotron photons can produce e^+e^- pairs in the magnetic field, giving

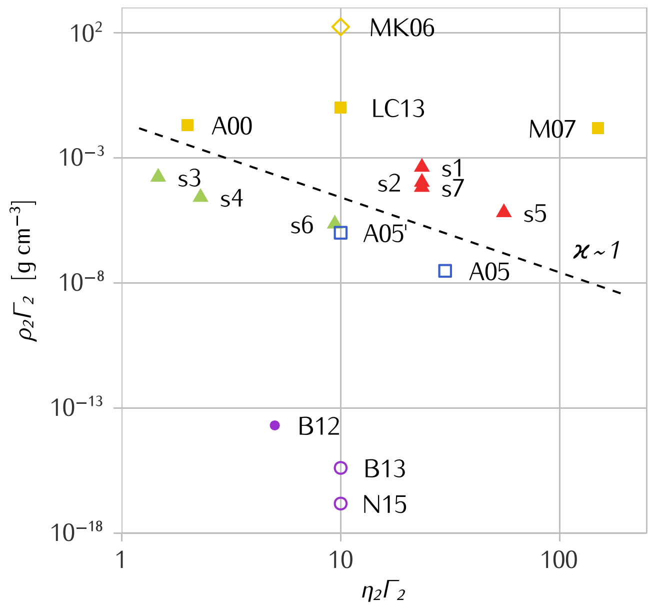

Figure 7. Parameters of counterstreaming plasma flows. A subset of the simulations (this paper; red triangles: s1, s2, s5, and s7) demonstrates copious pair production and significant synchrotron losses, whereas in the other simulations of this paper (green triangles: s3, s4, s6) the positron yield is low and the energy of the synchrotron photons does not much exceed the energy of the magnetic field. These subsets evidently belong to the regions $\varkappa > 1$ (above the dashed line) and $\varkappa < 1$ (below it), respectively (for $\varkappa$, see Equation (45) and Table 1). A number of numerical models of GRBs (collapsars with neutrino–antineutrino annihilation powered jets (yellow squares: A00, LC13, and M07), mergers (hollow blue squares: A05 and A05′), a collapsar with a Blandford–Znajek powered jet (a hollow yellow diamond: MK06)) found in the literature, as well as the estimated properties of a tidal disruption event leading to jet formation (solid circle B12) and blazars (hollow circles B13 and N15) are also shown (see the text for details).

the number of positrons up to 10^{-3} and higher for the number of electrons in the flows. In order to clarify the flow parameters leading to copious pair production, the theoretical estimate, Equation (42), can be rewritten using the rest-mass density of the hydrogen plasma of the flows ρ (namely, the density of the cooled plasma in the comoving reference frame):

$$\varkappa \sim 6.2 \times \eta_2^{3/2}\Gamma_2^2\sqrt{\rho_2[\mathrm{g\ cm^{-3}}]} \gtrsim 1, \qquad (45)$$

where the flow Lorentz factors $\Gamma_{1,2}$ are given in the center-of-momentum reference frame (see Equation (37)) and $\eta = (\overline{\gamma'} - 1)$ is the mean normalized kinetic energy of the ions in the reference frame comoving with the flow. The index 2 denotes the flow with particle density lower than the density of the other flow, i.e., $n_2 \leqslant n_1$. For instance, this estimate yields $\varkappa \approx 1$ for $\eta_2 \sim 1$, $\Gamma_2 = 5$, and $\rho_2 \sim 10^{-4}$ g cm^{-3}.

The simulation results s1–s7 are obtained for M/m far from the real proton-to-electron mass ratio ($\approx$1836), but can be scaled in a way that conserves the base estimate (42) as follows: $\eta_2\Gamma_2$ from Table 1 is multiplied by $aM/(1836m)$, and n_2 is replaced by n_2/a^3, where a is an arbitrary constant (we choose $a = 10^{4/3}$ in order to fit $\eta_2\Gamma_2$ in the range 1–100). The values of $\eta_2\Gamma_2$ and n_2 obtained with this scaling correspond to a hydrogen plasma and can be tested with criterion (45) and compared with the generally assumed values of these parameters for astrophysical jets.

The line corresponding to Equation (45) and $\varkappa \sim 1$, along with the points obtained from the simulation results s1–s7, are shown in Figure 7. The simulations s1, s2, s7, and s5, resulting in a high number of positrons and high rate of their production, are marked with red triangles. The simulations s3, s4 and s6, resulting in a low number of positrons generated, are marked with green triangles. It is clearly seen that the line $\varkappa \sim 1$ divides well the regions of copious and weak positron production, and Equation (45) can be used to test various astrophysical objects.

4.1. Gamma-Ray Bursts

Relativistic plasma jets are often associated with GRBs, tidal disruption events, active galactic nuclei (AGNs), and blazars. The energy of particles in the jets and the jet mass density could not be measured directly; however, the values used in a number of models of these phenomena can be used.

In the collapsar model of MacFadyen & Woosley (MacFadyen & Woosley 1999; Woosley & MacFadyen 1999), GRBs are linked with rotating massive stars, the core collapse of which produce a black hole swallowing surrounding matter. In that process, strong jets are generated due to energy deposition in the progenitor star envelope within the cone region around the rotation axis of the star. This energy deposition can be associated with neutrino–antineutrino annihilation with subsequent heating and acceleration of the baryonic matter. The Weibel instability can arise either in internal shocks in the jets or in external shocks with a pre-explosive stellar wind or the star envelope. Note that in this model the huge external pressure that accelerates the jets is often associated not with the ion temperature but mostly with radiation, hence we use $\eta \sim 1$ for this model. Note that such an assumption neglects the e^+e^- pairs produced by neutrino–antineutrino annihilation and contributing to the plasma density, hence the parameter $\varkappa$ given for the collapsar models below is rather underestimated.

In the simulations based on the MacFadyen & Woosley model (Aloy et al. 2000) with energy deposition of the order of 10^{50}–10^{51} erg, the jet breaking out of the progenitor star has the rest-mass density of about 10^{-1} g cm^{-3}, the temperature $\eta \sim 1$, and the Lorentz factor $\Gamma \sim 5$, while the envelope of the star is motionless and has a density of about 1 g cm^{-3} (see dotted lines in Figure 2 from Aloy et al. 2000). In the center-of-momentum reference frame, the Lorentz factor of the less dense flow (the jet) can be estimated as $\Gamma_2 \sim 2$, while the rest-mass density and thermal energy of ions, obviously, are the same, $\rho_2 \sim 10^{-2}$ g cm^{-3} and $\eta_2 \sim 1$. These parameters yield $\varkappa \approx 2.5$ and are shown as the yellow square A00 in Figure 7.

In the two-dimensional simulation of Morsony et al. (2007), adhering to the MacFadyen & Woosley collapsar model and a power-law stellar envelope model, the energetic jet ($\Gamma \approx 300$, $\rho \sim 10^{-4}$ g cm^{-3}; see the color version of Figure 3 in Morsony et al. 2007) breaks out of the star envelope ($\rho \sim 10^{-1}$ g cm^{-3}) that provides favorable conditions for the extreme Weibel instability ($\Gamma_2 \sim 150$, $\eta_2 \sim 1$, $\rho_2 \sim 10^{-4}$ g cm^{-3}, $\varkappa \approx 10^3$; see the yellow square M07 in Figure 7). In a further development of this model (three-dimensional simulation with a more realistic stellar progenitor; see López-Cámara et al. 2013), the parameters of the jet breaking out of the progenitor star (at $t = 4.2$ s) are slightly different: the jet has $\Gamma \approx 10$ and $\rho \sim 10^{-2}$ g cm^{-3}, and the envelope has $\rho \sim 1$ g cm^{-3} (see the green lines in Figures 4 and 6 of López-Cámara et al. 2013). These parameters yield $\Gamma_2 \sim 10$ and $\rho_2 \sim 10^{-2}$ g cm^{-3} (shown in Figure 7 as the LC13 yellow square), which, together with $\eta \sim 1$, are above the threshold $\varkappa \sim 1$ ($\varkappa \approx 60$).

Short GRBs are not linked with supernova explosions, and it is proposed that mergers (neutron star–neutron star or neutron star–black hole mergers) could be the source of such bursts. It implies lower density of the ambient and the jet plasmas, and higher Lorentz factors of the jets in general (Aloy et al. 2005). For instance, in the simulation B01 at time 0.5 s (see Figures 25 and 26 of Aloy et al. 2005), the Lorentz factor of the jet head is $\Gamma \approx 1000$ and its rest-mass density is only $\rho \sim 10^{-9}$ g cm^{-3}. Assuming that the internal shock in such a jet has $\Gamma_2 \sim \Gamma^{1/2} \approx 30$ (A05 hollow blue square in Figure 7), we obtain $\varkappa \approx 0.2$. Earlier, i.e., at time 0.1 s, the head of the jet has the Lorentz factor $\Gamma \sim 100$ and density $\rho \sim 10^{-7}$ g cm^{-3} (see Figures 15 and 16 of Aloy et al. 2005). The corresponding parameters of the internal shock with $\Gamma_2 \sim \Gamma^{1/2} \approx 10$ again are not favorable for pair production during the Weibel instability ($\varkappa \approx 0.2$) and are shown as the A05 hollow blue square in Figure 7.

Another model of jet formation in long GRB engines connects it with the Blandford–Znajek mechanism of energy extraction from a rotating black hole (Blandford & Znajek 1977) and predicts the formation of a magnetically driven outflow McKinney (2006; i.e., an outflow with magnetic pressure dominating over particle pressure and Poynting flux dominating over the flux of the particle energy). This model allows one to estimate the plasma density if the GRB luminosity and the mass of the central black hole is known (see the next subsection for details). For example, for a black hole with mass $M_{\rm BH} = 10\,M_\odot$ (where $M_\odot$ is the solar mass) and overall jet luminosity $L_j = 10^{50}$ erg s^{-1}, which is typical for long GRBs (Piran 1999), one can obtain a huge density $\rho_2 \sim 17$ g cm^{-3} that together with $\Gamma_2 \approx 10$ leads to $\varkappa \sim 10^3$ and is shown as the MK06 hollow yellow diamond in Figure 7.

Thus, the pair production regime of the Weibel instability can potentially be reached in long GRBs associated with the collapse of massive stars. Short GRBs associated with the merging of black holes and neutron stars presumably provide $\varkappa \lesssim 1$ and a negligible rate of pair production in the magnetic field of collisionless shocks.

4.2. Supermassive Black Holes

It is generally believed that supermassive black holes (SMBHs) drive energetic outflows in AGNs and blazars. However, a large value of the Schwarzschild radius of SMBHs implies a low value of the plasma density and $\varkappa \ll 1$.

The source Swift J164449.3+573451, which is associated with a tidal disruption of a star by a dormant SMBH (Zauderer et al. 2011), is of interest because the observable data allows one to estimate the jet parameters quite near the black hole. The rapid time variability of the gamma-rays and X-rays requires a compact source with a characteristic size of $\lesssim$0.15 au ($\lesssim 2 \times 10^{12}$ cm; Berger et al. 2012). More than 200 days of radio observations of the source let one obtain the jet properties at the distance $r_{rf} \sim 10^{18}$ cm from the black hole (Berger et al. 2012): $\Gamma \approx 5$ and $n(r_{rf}) \sim 1$ cm^{-3}. Assuming that the opening angle of the jet $\theta_j \sim 5°$, the distance between the SMBH and the gamma- and X-ray source is $r_\gamma \sim (\tan\theta_j)^{-1} \times 0.15$ au $\sim 2 \times 10^{13}$ cm, which yields at this distance $n(r_\gamma) \sim n(r_{rf}) r_{rf}^2 / r_\gamma^2 \sim 2.5 \times 10^9$ cm^{-3}, hence $\rho_2 \sim 4 \times 10^{-15}$g cm^{-3}. This value, together with $\Gamma_2 \approx 5$ and $\eta_2 \approx 1$, gives $\varkappa \sim 10^{-5}$, and is depicted as the B12 violet circle in Figure 7.

The parameters of the blazar jets can be similarly found from radio observations and the luminosity in all bands, and then can be continued up to the distance closer to the central black hole. The distance from the black hole r_γ where the internal shock and the Weibel instability arise is crucial for a plasma density estimate and can be found as follows. First, r_γ is connected with the variability timescale $t_{\rm var}$ and the jet opening angle θ_j, $r_\gamma \sim ct_{\rm var}(\tan\theta_j)^{-1}$. Second, the numerical hydrodynamical model of jet formation of McKinney (2006), which takes into account general relativity and is capable of modeling the Blandford–Znajek mechanism of the jet supply (Blandford & Znajek 1977), predicts that magnetic pressure dominates in the jet from the region of jet formation up to the Alfvén surface at $r_A \sim 10\text{–}100\, r_g$, where $r_g = 2GM_{\rm BH}/c^2$ is the black hole Schwarzschild radius, $M_{\rm BH}$ is the black hole mass, and G is the gravitational constant. Beneath the Alfvén surface, the internal shocks are absent in the simulations of McKinney (2006), hence $r_\gamma \geqslant r_A \sim 100 r_g$.

Let us assume that the jet luminosity L_j is equal to the jet energy traveling through the jet cross-section at r_γ, and the particle energy becomes comparable with the energy of the magnetic field here, hence

$$L_j \sim \pi {r_\gamma}^2 \rho c^3 \eta \Gamma^2 \tan^2\theta_j. \tag{46}$$

Thus, in order to estimate ρ, one should know $M_{\rm BH}$, Γ, and η. Relying on the simulations of McKinney (2006), we use $\Gamma \approx 10$ and $\theta_j \approx 5°$ in further estimations, additionally assuming $\eta \sim 1$.

In order to estimate the parameters of the internal shock that is the nearest to the black hole of the famous blazar 3C 273, we follow Böttcher et al. (2013) and Zdziarski & Böttcher (2015). In the leptonic model of Böttcher et al. (2013), $L_j \approx 1.3 \times 10^{46}$ erg s^{-1} (see Equation (5) and the value of L_p in Table 2 therein), and in Zdziarski & Böttcher (2015), the black hole mass is assumed to be $M_{\rm BH} \approx 7 \times 10^9\, M_\odot$, which yields $r_\gamma = 2 \times 10^{15}$ cm, $\rho \approx 4 \times 10^{-17}$ g cm^{-3}, and $\varkappa \sim 10^{-6}$ (see the B13 hollow violet circle in Figure 7). Note that the variability timescale $t_{\rm var} \sim 1$ day gives a slightly higher value of $r_\gamma \sim 3 \times 10^{16}$ cm and an even lower value of $\varkappa$.

The reported detection of gravitational lensing of the blazar PKS 1830–211 (Neronov et al. 2015) independently provides the size of the gamma-ray emitting region about $r_\gamma/\tan\theta_j \sim 10^{15}$ cm, which coincides fairly well with about a 1 day variability timescale and 10–100 r_g for the central black hole (Neronov et al. 2015). Thus, we adopt $r_\gamma \sim 10^{16}$ cm, which, together with the luminosity $L_j \sim 3 \times 10^{45}$ erg s^{-1}, leads to $\rho \sim 1.5 \times 10^{-18}$ g cm^{-3} and $\varkappa \sim 10^{-6}$ (see the N15 violet hollow circle in Figure 7).

Therefore, SMBHs provides outflows with very low plasma density and $\varkappa \ll 1$.

4.3. Collisions

Figure 7 clearly demonstrates that the copious emission of hard photons and pair production during the Weibel instability rises if the plasma density is at least 10^{-8} g cm^{-3}. In such plasmas, electron–photon and electron–ion collisions can be important, and the corresponding cross-sections should be estimated.

The Compton scattering cross-section in the center-of-momentum reference frame can be estimated as follows (Berestetskii et al. 1982):

$$\sigma_C \sim \frac{r_e^2}{\bar\gamma^2} \ln\bar\gamma, \tag{47}$$

where $r_e = e^2/(mc^2)$ is the classical electron radius, and the electron and photon energies are approximately equal to each other and to $\bar\gamma mc^2$. Thus, the ratio of the free time $t_f^{(C)} = 1/nc\sigma_C$ (the mean time between two scattering events of the same particle) to the Weibel instability timescale Λ_m^{-1} (36) is

$$\Lambda_m t_f^{(C)} \sim \frac{\bar\gamma^{3/2}}{\ln\bar\gamma} \frac{\lambda}{r_e} \gg 1 \tag{48}$$

for almost any realistic plasma density (here λ is the plasma wavelength).

Electron–proton scattering can be considered similarly. The momentum-transfer (transport) cross-section σ_{mt} is determined mostly by events with little change in the particle directions, and formulas for electron scattering in a constant field can be used (Landau & Lifshitz 1975, 1976; Berestetskii et al. 1982):

$$\sigma_{mt} \approx \frac{8\pi r_e^2}{\gamma_0^2} \ln\frac{\theta_{\max}}{\theta_{\min}}, \tag{49}$$

where $\theta_{\max}$ and $\theta_{\min}$ are the maximum and minimum deflection angles of the electron trajectory, respectively, and γ_0 is the initial Lorentz factor of the scattered electron. In the limit $\theta \ll 1$, the angles can be estimated as (Landau & Lifshitz 1975)

$$\theta \approx \frac{2r_e}{\gamma_0 r_0}, \tag{50}$$

where r_0 is the impact parameter. The minimal deflection angle $\theta_{\min}$ can be estimated using the Debye length $r_D \sim c\bar\gamma^{1/2}/\omega_p$, and, as long as the electron de Broglie wavelength is smaller than the proton size ($\sim r_e$; we assume $\gamma_0 \gtrsim \hbar c/e^2 \approx 137$), the maximal deflection angle can be estimated using the proton size. Therefore, we estimate the momentum-transfer cross-section as follows:

$$\sigma_{mt} \sim \frac{8\pi r_e^2}{\gamma_0^2} \ln\frac{\lambda\bar\gamma^{1/2}}{r_e}, \tag{51}$$

and the ratio of the corresponding timescale $t_f^{(ei)}$ to the timescale of the Weibel instability (36) as follows:

$$\Lambda_m t_f^{(ei)} \sim \frac{\lambda}{r_e}\bar\gamma^{3/2} \ln^{-1}\frac{\bar\gamma^{1/2}\lambda}{r_e}, \tag{52}$$

This ratio is smaller than $\Lambda_m t_f^{(C)}$ by a logarithmic factor of the order of 10, thus $\Lambda_m t_f^{(ei)}$ is also much greater than unity for almost all plasma parameters.

The characteristic timescale of electron energy losses caused by bremsstrahlung is about the timescale of e^+e^- pair production by a photon colliding with a proton (Berestetskii et al. 1982), and is the following:

$$\Lambda_m t_f^{(b)} \sim \frac{1}{\alpha\bar\gamma^{1/2}\ln\bar\gamma} \frac{\lambda}{r_e}, \tag{53}$$

where $\bar\gamma$ is the Lorentz factor of the emitting electron or the energy of the photon-producing e^+e^- pair, normalized to mc^2.

For the density $\rho \sim 10^{-4}$ g cm^{-3} and $\bar{\gamma} = 1.8 \times 10^4$ providing $\varkappa \sim 1$, we have $\Lambda_m t_f^{(b)} \sim 10^8 \gg 1$.

Therefore, for the parameters of interest, the effect of collisions is negligible on the Weibel instability timescale. However, at least the scale $ct_f^{(b)}$ is less than the size of a gamma-ray emitting region in the collapsar model of GRBs. Namely, for a photon density of the order of $n_1 \sim n_2$, and $\rho_{1,2} \sim 10^{-4}$ g cm^{-3}, $\eta_{1,2} \sim 1$, and $\Gamma_{1,2} \sim 10$, we obtain $ct_f^{(C)} \sim 10^{13}$ cm $\gg r_\gamma$, $ct_f^{(ei)} \sim 10^{12}$ cm $\gg r_\gamma$, and $ct_f^{(b)} \sim 10^6$ cm $\ll r_\gamma$ for both $\nu\tilde{\nu}$-annihilation driven jet (r_γ is less than or about 1 light-second) and a jet driven by the Blandford–Znajek mechanism ($r_\gamma \sim 10^7$ cm).

Therefore, the spectral energy distribution (SED) of photons would be drastically modified as they disappear in the e^+e^- photoproduction in collisions with the nucleus. The cross-section of this process for high-energy photons ($\bar{\gamma} \gg 1$) depends logarithmically on the photon energy, and the threshold of the pair photoproduction $\bar{\gamma} \sim 1$ should be distinguished in the SED. Indeed, *Fermi* GBM data demonstrate that most SEDs of the detected GRBs have a break in the power-law fit (Gruber et al. 2014) or a maximum in the photon energy distribution (Abdo et al. 2009) at 100–1000 keV. The maximum photon energy detected in GRBs (tens of GeV; see Abdo et al. 2009; Ackermann et al. 2014) is about the energy of a proton with a Lorentz factor of about 100 that coincides well with the generally believed Lorentz factor of GRB jets. In any case, the generation of observed high-energy photons can hardly be attributed to the high-density shock-wave region because of the complicated energy–temporal distribution of the photons (Abdo et al. 2009; Ackermann et al. 2014). Moreover, blazars also emit photons with energy ~10 GeV; nevertheless, they have no regions of high-density plasma (see Figure 7) that imply other mechanisms of high-energy photons generation (e.g., Comptonization).

Thus, collisional effects are negligible on the timescale of the Weibel instability; however, bremsstrahlung as well as pair production in photon–proton collisions should be taken into account on the scale of the gamma-ray emitting region of GRBs.

5. Summary

The Weibel instability in hot and dense counterstreaming relativistic plasma flows is considered theoretically and numerically. The results include the following.

(i) Due to the relativistic pinch of the angles, if the flow's Lorentz factor $\Gamma \gg 1$, the instability scenario for hot plasma is the same as for the cold one, namely, current filaments elongated in the direction of the flow's velocity, and the magnetic field focusing the filaments, are formed.

(ii) Numerical simulations reveal that the generated magnetic field causes an efficient synchrotron emission by electrons, and the overall energy of the synchrotron photons can be much higher than the energy of the magnetic field.

(iii) At the linear stage of the instability, the transverse filament scale λ_m and the instability growth rate Λ_m can be estimated using Equations (35) and (36), even if synchrotron losses are considerable. For a certain Lorentz factor of the flows Γ and for a proper flow temperature ($\propto\eta$), one can find $\Lambda_m \propto (\eta\Gamma)^{-1/2}$ and $\lambda_m \propto (\eta/\Gamma)^{1/2}$.

(iv) Pair photoproduction in the magnetic field can efficiently convert the synchrotron photons to e^+e^- pairs. The criterion for judging copious pair production in the Weibel instability is proposed ($\varkappa \gtrsim 1$; see Equations (42) and (45)). Moreover, the fulfillment of this criterion also ensures that the energy of synchrotron photons is greater than the magnetic field energy (ii).

(v) The considered effects become noticeable for plasmas with very high values of the mean electron Lorentz factor, which leads to the timescale of the collisional effects being much longer than the instability timescale.

(vi) In the framework of the collapsar model of long GRBs, $\varkappa \gtrsim 1$ and even $\varkappa \gg 1$ can be reached for the interaction of the jet with the progenitor star envelope, or for the internal shock in the jet at a distance of about 100 Schwarzschild radii from the black hole (see Figure 7).

The Weibel instability that leads to $\varkappa \gg 1$ should potentially modify the plasma parameters dramatically. The gamma-ray emission and the e^+e^- pair photoproduction would not stop until the mean particle energy becomes so low that $\varkappa \lesssim 1$. Therefore, in the shock region, the plasma density can be increased a lot, which at the same time leads to the decrease of the mean particle energy. The impact of this scenario on the GRB models will be considered elsewhere.

This research was supported by the Russian Foundation for Basic Research (grant No. 15-02-06079), by the Grants Council under the President of the Russian Federation (grant No. MK-2218.2017.2), and by the "Basis" Foundation (grant No. 17-11-101).

We thank Vl. V. Kocharovsky for inspiring conversations and I. I. Artemenko for a discussion on the effect of collisions.

Software: QUILL (Nerush & Kostyukov 2010; Serebryakov et al. 2015; http://iapras.ru/english/structure/dep_330/quill.html), ggplot2 (Wickham 2016; http://ggplot2.org/).

ORCID iDs

E. N. Nerush https://orcid.org/0000-0003-4227-9233
D. A. Serebryakov https://orcid.org/0000-0001-9233-7214
I. Yu. Kostyukov https://orcid.org/0000-0002-5818-440X

References

Abdo, A. A., Ackermann, M., Arimoto, M., et al. 2009, Sci, 323, 1688
Ackermann, M., Ajello, M., Asano, K., et al. 2014, Sci, 343, 42
Aloy, M. A., Janka, H.-T., & Müller, E. 2005, A&A, 436, 273
Aloy, M. A., Müller, E., Ibáñez, J. M., Martí, J. M., & MacFadyen, A. 2000, ApJ, 531, L119
Artemenko, I. I., Golovanov, A. A., Kostyukov, I. Y., et al. 2016, JETPL, 104, 883
Baier, V. N., Katkov, V., & Strakhovenko, V. 1998, Electromagnetic Processes at High Energies in Oriented Single Crystals (Singapore: World Scientific)
Berestetskii, V. B., Lifshitz, E. M., & Pitaevskii, L. P. 1982, Quantum Electrodynamics (New York: Pergamon)
Berger, E., Zauderer, A., Pooley, G. G., et al. 2012, ApJ, 748, 36
Birdsall, C. K., & Langdon, A. B. 2004, Plasma Physics via Computer Simulation (Boca Raton, FL: CRC Press)
Blandford, R. D., & Znajek, R. L. 1977, MNRAS, 179, 433
Böttcher, M., Reimer, A., Sweeney, K., & Prakash, A. 2013, ApJ, 768, 54
Chevalier, R. A. 1998, ApJ, 499, 810
Efimenko, E., Bashinov, A., Bastrakov, S., et al. 2017, arXiv:1708.09636
Elkina, N. V., Fedotov, A. M., Kostyukov, I. Y., et al. 2011, PhRvS, 14, 054401
Garasev, M., & Derishev, E. 2016, MNRAS, 461, 641
Garasev, M. A., Korytin, A. I., Kocharovsky, V. V., et al. 2017, JETPL, 105, 164

Gonoskov, A., Bastrakov, S., Efimenko, E., et al. 2015, PhRvE, 92, 023305
Grassi, A., Grech, M., Amiranoff, F., et al. 2017, PhRvE, 95, 023203
Grismayer, T., Vranic, M., Martins, J. L., Fonseca, R. A., & Silva, L. O. 2017, PhRvE, 95, 023210
Gruber, D., Goldstein, A., Weller von Ahlefeld, V., et al. 2014, ApJS, 211, 12
Huntington, C. M., Fiuza, F., Ross, J. S., et al. 2015, NatPh, 11, 173
Kalapotharakos, C., Brambilla, G., Timokhin, A., Harding, A. K., & Kazanas, D. 2017, arXiv:1710.03170
Landau, L., & Lifshitz, E. 1976, Mechanics (3rd ed.; Portsmouth, NH: Butterworth-Heinemann)
Landau, L. D., & Lifshitz, E. M. 1975, The Classical Theory of Fields (Oxford: Elsevier)
Liu, X., Li, Y. T., Zhang, Y., et al. 2011, NJPh, 13, 093001
López-Cámara, D., Morsony, B. J., Begelman, M. C., & Lazzati, D. 2013, ApJ, 767, 19
MacFadyen, A. I., & Woosley, S. E. 1999, ApJ, 524, 262
McKinney, J. C. 2006, MNRAS, 368, 1561
Medvedev, M. V., Fiore, M., Fonseca, R. A., Silva, L. O., & Mori, W. B. 2005, ApJL, 618, L75
Morsony, B. J., Lazzati, D., & Begelman, M. C. 2007, ApJ, 665, 569
Neronov, A., Vovk, I., & Malyshev, D. 2015, NatPh, 11, 664
Nerush, E., & Kostyukov, I. Y. 2010, VANT, 68, 3 (http://vant.kipt.kharkov.ua/ANNOTAZII_2010/annotazii_2010_4_3.html)
Nerush, E. N., & Kostyukov, I. Y. 2015, PPCF, 57, 035007
Nerush, E. N., Kostyukov, I. Y., Fedotov, A. M., et al. 2011, PhRvL, 106, 035001
Nerush, E. N., Kostyukov, I. Y., Ji, L., & Pukhov, A. 2014, PhPl, 21, 013109
Nishikawa, K.-I., Niemiec, J., Hardee, P. E., et al. 2009, ApJL, 698, L10
Piran, T. 1999, PhR, 314, 575
Pukhov, A. 1999, JPlPh, 61, 425
Pukhov, A. 2003, RPPh, 66, 47
Saito, S., & Sakai, J.-I. 2004, PhPl, 11, 859
Serebryakov, D. A., Nerush, E. N., & Kostyukov, I. Y. 2015, PhPl, 22, 123119
Silva, L. O., Fonseca, R. A., & Tonge, J. W. 2003, ApJL, 596, L121
Soderberg, A. M., Chakraborti, S., Pignata, G., et al. 2010, Natur, 463, 513
Spitkovsky, A. 2008, ApJL, 682, L5
Stockem, A., Fiuza, F., Bret, A., Fonseca, R. A., & Silva, L. O. 2014, NatSR, 4, 3934
Timokhin, A. N. 2010, MNRAS, 408, 2092
Vay, J.-L. 2008, PhPl, 15, 056701
Weibel, E. S. 1959, PhRvL, 2, 83
Wickham, H. 2016, ggplot2: Elegant Graphics for Data Analysis (Berlin: Springer)
Woosley, S. E., & MacFadyen, A. I. 1999, A&AS, 138, 499
Zauderer, B. A., Berger, E., Soderberg, A. M., et al. 2011, Natur, 476, 425
Zdziarski, A. A., & Böttcher, M. 2015, MNRAS Letters, 450, L21